Scientific paper

Magnetically Separable Ag/$CuFe_2O_4$/Reduced Graphene Oxide Ternary Nanocomposite with High Performance for the Removal of Nitrophenols and Dye Pollutants from Aqueous Media

Ladan Nirumand, Saeed Farhadi* and Abedin Zabardasti

Department of Chemistry, Lorestan University, Khorramabad 68135-465, Iran

** Corresponding author: E-mail: sfarhadi1348@yahoo.com (S. Farhadi)*
Tel.: +986633120611; Fax: +986633120618

Received: 05-07-2018

Abstract

In this work, a novel ternary magnetic nanocomposite namely Ag/$CuFe_2O_4$/rGO was produced by a facile solvothermal route. The reduction of graphene oxide (GO) to reduced form (rGO) and the in-situ deposition of $CuFe_2O_4$ and Ag nanoparticles on rGO occurred simultaneously in a one-pot reaction. The structure, composition and morphology of the as-prepared nanocomposite were characterized by FT-IR, XRD, VSM, FESEM, EDX, TEM, and BET analyses. The results indicated that the Ag and $CuFe_2O_4$ nanoparticles were successfully loaded on the surface of rGO. The catalytic performance of the Ag/$CuFe_2O_4$/rGO nanocomposite was evaluated for the reduction of nitroarenes to corresponding amines in the presence of sodium borohydride ($NaBH_4$) as a reducing agent. The nanocomposite exhibited the high performance in the reduction of the reduction of nitroarenes with 100% conversion within 10–30 min. The catalytic activity of the Ag/$CuFe_2O_4$/rGO was enhanced compared with Ag/$CuFe_2O_4$, Ag/rGO and $CuFe_2O_4$/rGO samples due to easier electron transfer process. Furthermore, the adsorption data revealed that cationic methylene blue (MB) dye could be removed almost completely on the Ag/$CuFe_2O_4$/rGO composite within 2 min and the composite could also selectively adsorb MB from the mixed solution with anionic methyl orange (MO). Due to the existence of magnetic $CuFe_2O_4$ nanoparticles, the Ag/$CuFe_2O_4$/rGO nanocomposite can be magnetically separated and reused without any change in structure and performance.

Keywords: Graphene oxide nanosheets; Silver nanoparticles; Ternary magnetic nanocomposite; Nitrophenols reduction; Dyes adsorption

1. Introduction

Nitroarenes are one of the most common pollutants that often exist in industrial wastewaters, while aromatic amines are of various commercial importance as an intermediate for the production of pharmaceutical ingredients, various polymers and dyes.[1–3] In fact, synthesis of aminoarenes from the corresponding nitro compounds is an important process in the chemical industries and several methods for preparation of them were found, such as stoichiometric reducing agents and catalytic hydrogenation.[4–7] A large amount of industrial wastewaters also contain organic dye pollutants. Organic dyes are one of the main causes of the pollution of industrial wastewater that removal of them through different technologies such as adsorption is of great importance in environmental processes.[8–15] Hence, there is a need to find a new desirable material, which not only has the capacity of reducing the nitroarenes but also can achieve adsorption and selective separation of organic pollutants. To date, many researches have been carried out in the area of metal nanoparticles-based heterogeneous catalysts as they possess a high surface to volume ratio and reusability, ease of separation and enhanced catalytic properties.[16–18] Among them, gold and silver nanoparticles are particularly attractive due to their high electrical, optical, and catalytic properties,[19–21] but they require suitable supports such as metal oxides, zeolites or graphene derivatives to immobilize them and prevent aggregation during the reaction.[22–25]

Graphene, single-layer carbon atoms densely packed into a two-dimensional (2D) lattice, has high surface area, excellent electrical conductivity and high mechanical

strength.[26] It can be used as a promising catalyst support on which the metal nanocatalysts can be stabilized and result in the further enhanced catalytic performance.[27,28] One of the applications of graphene-based materials is also the removal of organic dye pollutants from water.[29,30] Many polymeric and inorganic adsorbents such as carbon-based materials,[31] porous metal oxides,[32] clays,[33] chitosan,[34] zeolites,[35] and metal–organic frameworks (MOFs)[36] have developed for adsorption removal of pollutants from aqueous solutions. Among them, carbonous materials such as graphene have shown excellent performance in adsorption of organic contaminants from water. However, such adsorbents are usually separated by tedious filtrating from water after the adsorption/catalytic process. To overcome this weakness, coupling with magnetic materials is highly desirable. Spinel ferrites with general formula MFe_2O_4 (M = Mn, Fe, Co, Ni, Cu, etc.) have been of great interest in many magnetic applications.[37]

Considering the above, in this work, we have synthesized the novel magnetic Ag/$CuFe_2O_4$/rGO ternary nanocomposite via solvothermal method which fully characterized by various spectroscopic techniques. During the formation of the composite, the reduction of graphene oxide (GO) to rGO and the in-situ deposition of $CuFe_2O_4$ and Ag nanoparticles on rGO occurred simultaneously in a one-pot reaction. Due to high catalytic activity of Ag, the nanocomposite displayed excellent performance for catalytic reduction of nitroarenes by using $NaBH_4$ in aqueous solutions. Also, owing to the existence of graphene with high surface area and adsorption capacity, the Ag/$CuFe_2O_4$/rGO nanocomposite exhibited high performance on the removal of dye pollutants from wastewater. Moreover, the magnetic properties of $CuFe_2O_4$ make the separation of the nanocomposite easier, avoiding environmental contamination from processing.

2. Experimental

2. 1. Materials

All reagents including solvents and all materials used for the synthesis of nanocomposite, 2-nitrophenol (2-NP), 4-nitrophenol (4-NP), 2-nitroaniline (2-NA), 4-nitroaniline (4-NA), sodium borohydride ($NaBH_4$), methylene blue (MB) and methyl orange (MO) were purchased from Merck or Sigma-Aldrich company with high purity (≥ 98%) and used without further purification.

2. 2. Preparation of Ag/$CuFe_2O_4$/rGO Nanocomposite

Graphene oxide (GO) nanosheets were prepared from natural graphite powder by a modified Hummer's method.[38] The graphite oxide layers were separated from each other through ultrasonication to acquire graphene oxide sheets. For synthesis of the Ag/$CuFe_2O_4$/rGO nanocomposite, the as-prepared GO (0.1 g), $Fe(NO_3)_3$ $9H_2O$ (2 mmol, 0.40 g) and $Cu(NO_3)_2$ $3H_2O$ (1 mmol, 0.12 g) were dispersed in 30 mL of ethylene glycol (EG) to form a clear solution, followed by the addition of sodium acetate (45 mmol, 3.10 g) and $AgNO_3$ (1.2 mmol, 0.20 g).The mixture was ultrasonicated for 120 min. Subsequently, the obtained suspension was transferred into a Teflon-lined stainless-steel autoclave. The autoclave was sealed and put into the oven, which was heated and maintained at 200 °C for 9 h, then taken out and allowed to cool naturally at room temperature. Finally, the black product was magnetically collected and washed thoroughly with water and ethanol, followed by drying at 50 °C for a few hours. It was denoted as Ag/$CuFe_2O_4$/rGO nanocomposite with 23 wt% Ag as confirmed by ICP-AES analysis. For comparison, Ag/$CuFe_2O_4$, Ag/rGO and $CuFe_2O_4$/rGO samples were synthesized under the same conditions in the absence of rGO, $CuFe_2O_4$ and Ag, respectively. Also, the samples of rGO and Ag nanoparticles were prepared via the reduction of GO (0.1 g) and $AgNO_3$ (0.2 g), respectively, in 30 mL of ethylene glycol (EG) as solvent and reducing agent under hydrothermal conditions at 200 °C for 9 h.

2. 3. Characterization Techniques

X-ray diffraction (XRD) measurements were carried out on a Rikagu D-max X-Ray diffractometer using Cu Kα radiation (λ = 1.540 Å). Fourier transform infrared (FT-IR) spectra were recorded using Shimadzu FT- IR 160 spectrometer over the wavenumber range from 4000 to 400 cm^{-1}. Raman spectra were obtained using a Raman microscope with laser wavelength of 785 nm. The morphology and size of the nanocomposite particles were characterized by Mira3 Tescan, scanning electron microscope (FESEM) outfitted with energy field dispersive X-ray analyzer (EDX) for the elemental analysis of the sample. TEM images were obtained on the electron microscope (Philips CM120) at the accelerating voltage of 100 kV. The magnetic properties were measured using a vibrating sample magnetometer (Model: MDKFD, Magnetic Daneshpajoh Kashan Co., Iran) with a maximum magnetic field of 10 kOe. The Brunauer-Emmett-Teller (BET) surface area was measured by N_2 adsorption measurements at 77 K using Belsorp mini apparatus. UV-visible spectra were obtained from a Cary 100 Varian spectrophotometer in a wavelength range of 200–800 nm. The concentration of metals in the filtrate was determined by inductively coupled plasma atomic emission spectroscopy (Perkin Elmer ICP-AES).

2. 4. Catalytic Reduction Tests

In order to study the catalytic performance of as-synthesized Ag/$CuFe_2O_4$/rGO nanocomposite in reductive processes, the reduction of some nitroaromatic compounds to corresponding amino derivatives by excess

$NaBH_4$ in aqueous solution was investigated. For this work, freshly prepared aqueous solution of $NaBH_4$ (0.5 mL, 20 mM) was mixed with as-prepared aqueous solution (3 mL, 0.2 mM) of the nitroaromatic compounds, in the quartz cell (1.0 cm path length and 4 mL volume). Then, 3 mg of the $Ag/CuFe_2O_4/rGO$ nanocatalyst was added into the solution and the progress of reduction was monitored by UV-Vis spectrophotometer in the range of 200–800 nm, with cycling over definite time intervals at room temperature.

2. 5. Dye Adsorption Tests

The adsorption experiments were performed as follows: 50 mg of the $Ag/CuFe_2O_4/rGO$ nanomaterial was added into 50 mL of dye solution (25 mg/L) under stirring. At predetermined time intervals, the concentrations of dye solutions, from which the adsorbent was removed by magnetic separation, were determined by measuring the absorbance of dye solution (MB,MO) using a Cary 100 Varian UV–Vis spectrophotometer. A similar experiment was also done with 50 mL of MB solutions with different concentrations (25, 50, 75 and 100 mg/L). Moreover, the UV–Vis spectroscopy was performed to determine the selective adsorption ability of $Ag/CuFe_2O_4/rGO$ nanocomposite at given time intervals. The amount of dye removal efficiency was calculated by the following equation:

Removal efficiency (%) = $(C_0\text{-}C_t)/C_0 \times 100$, where C_0 and C_t are the dye concentrations (mg/L) at the initial and t time, respectively. In all aqueous solutions containing dye and $Ag/CuFe_2O_4/rGO$ nanocomposite, the residual concentrations of Ag and Cu after removing the adsorbent were detected to be less than 0.1 wt% by ICP-AES analysis.

3. Results and Discussion

3. 1. Characterization of the $Ag/CuFe_2O_4/rGO$ Nanocomposite

The XRD analysis was used to investigate the composition and structure of the products. Figure 1 shows the XRD patterns of GO, rGO, $CuFe_2O_4$, Ag and $Ag/CuFe_2O_4/rGO$ samples. Figure 1(a) and (b) shows the XRD patterns of pure GO and GO after it was reduced in EG solvent under hydrothermal conditions. Figure 1(a) shows that GO exhibited a sharp and high-intensity diffraction peak at about $2\theta = 11.5°$. This result shows that a highly organized layer structure with an interlayer distance (d spacing) of 0.80 nm along the (002) orientation was produced. The (002) peak shifted to $2\theta = 21.5$ with d-spacing of 0.35 nm after reduction; thus, the d-spacing decreased from 0.80 nm to 0.35 nm. This decrease in d-spacing was caused by the elimination of oxygen-containing functional groups and H_2O molecules from the graphite interlayers during the reduction process. As seen in Figure 1(c), the diffraction peaks indexed at $2\theta = 30.2°$, 35.6°, 43.2°, 53.6°, 57.1°, 62.7° and 74.2° are attributed to (220), (311), (400), (107), (511), (440) and (533) planes of cubic spinel structure of $CuFe_2O_4$ (JCPDS-34-0425).[39] The XRD pattern of Ag nanoparticles in Figure 1(d) shows peaks at 2θ values of 38.3°, 43.5°, 64.6° and 77.5° which could be assigned to the (111), (200), (220) and (311) planes of metallic silver (JCPDS-04-0783).[40] From the XRD pattern of the $Ag/CuFe_2O_4/rGO$ nanocomposite (Figure 1(e)), it is clear that all appeared peaks can be attributed to $CuFe_2O_4$ and Ag phases. No characteristic diffraction peaks for rGO appeared in the pattern indicating that rGO nanosheets are not stacked during the nanocomposite formation process. The reason can be attributed to the fact that Ag and $CuFe_2O_4$ nanoparticles anchored on the surface of rGO nanosheets prevented the exfoliated rGO nanosheets from restacking.[41] The average particle size of nanocomposite was calculated to be about 27 nm using the classical Scherrer equation: $D_{XRD} = 0.9\lambda/(\beta\cos\theta)$, where D_{XRD} represents the crystallite size, λ is the wavelength of Cu Kα (0.154 nm), β is the full width at half maximum of the diffraction peak, and θ is the Bragg angle.

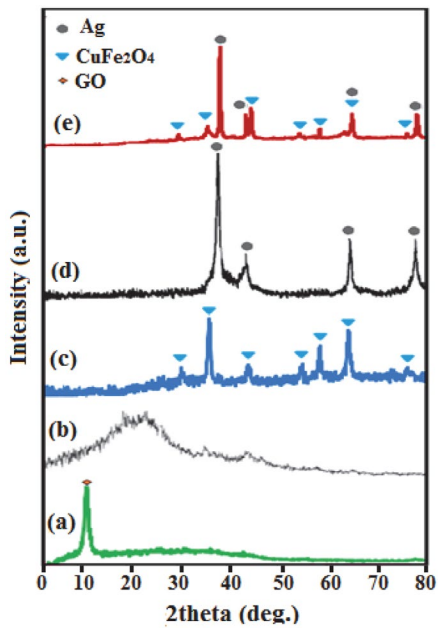

Figure 1. XRD patterns of (a) GO, (b) rGO, (c) $CuFe_2O_4$, (d) Ag and (e) $Ag/CuFe_2O_4/rGO$ samples.

FT-IR spectra of GO, rGO, $CuFe_2O_4$ and $Ag/CuFe_2O_4/rGO$ samples are shown in Figure 2. In FT-IR spectrum of GO (Figure 2(a)) obvious characteristic bands of GO could be seen, including C=O stretching vibrations of COOH groups (1727 cm^{-1}), graphitic C=C stretching vibrations (1618 cm^{-1}), O-H deformation vibrations of tertiary C-OH (1398 cm^{-1}), and C-O stretching vibrations of epoxy/alkoxy groups (1027 cm^{-1}).[42] After hydrothermal treatment of the pure GO in EG solvent, the band of C=O

was eliminated and the intensity of O-H and C-O bands were considerably decreased, which indicated the removal of oxygen-containing functional groups and reduction of GO (Figure 2(b)). In the case of pure $CuFe_2O_4$ (Figure 2(c)), the two characteristic bands appeared at 565 and 445 cm^{-1} are related to the stretching vibrations of M–O (M = Fe and Cu) bonds in the tetrahedral and octahedral sites of spinel-type oxide, respectively.[43,44] As can be seen in Figure 2(d), the characteristic band of rGO at 1615 cm^{-1} related to the graphitic C=C bond and the vibrational bands of $CuFe_2O_4$ in the range of 600–400 cm^{-1} were all observed in the IR spectrum of the nanocomposite sample which demonstrate the coexistence of rGO and $CuFe_2O_4$ in this hybrid nanomaterial. Moreover, the disappearance of the characteristic bands of GO confirms the formation of rGO in the nanocomposite and the restoration of a graphitic structure in graphene.[42]

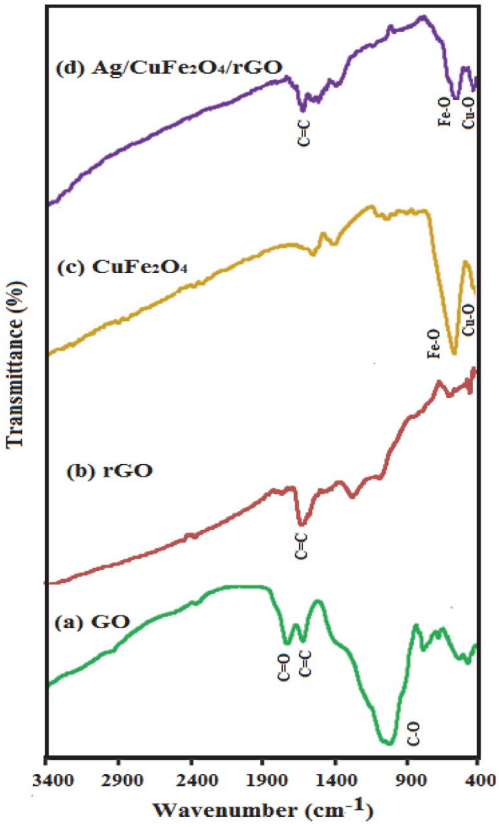

Figure 2. FT-IR spectra of (a) GO, (b) rGO, (c) $CuFe_2O_4$, and (d) $Ag/CuFe_2O_4$/rGO nanocomposite.

The morphology and microstructure of pure GO and $Ag/CuFe_2O_4$/rGO nanocomposite were investigated by SEM analysis. The SEM micrograph of pure GO in Figure 3(a) shows the highly porous and layered structure of GO having large stacks, possibly consisting of hundreds of GO nanosheets. It should also be noted that the surfaces of the GO sheets are quite flat and smooth. Figure 3(a) shows the SEM of GO nanosheets which stacked together due to the dispersive forces between them.[45] As can be seen in Figure 3(b), the surfaces of graphene nanosheets were covered with the agglomerated Ag and $CuFe_2O_4$ nanoparticles. It should also be noted that the pores between the graphene sheets were evenly filled up with the Ag and $CuFe_2O_4$ nanoparticles. In addition, the image of the nanocomposite clearly indicated that the surface properties of the modified GO product were strongly affected. Compared to pure GO, the surfaces of rGO nanosheets in the nanocomposite are rough, and the edges are highly crumpled.

Further investigation was carried out by energy dispersive X-ray spectroscopy (EDX) to characterize the composition of as-prepared $Ag/CuFe_2O_4$/rGO nanocomposite. The existence of Ag, Cu, Fe, C and O elements in the nanocomposite could be proved by the EDX elemental

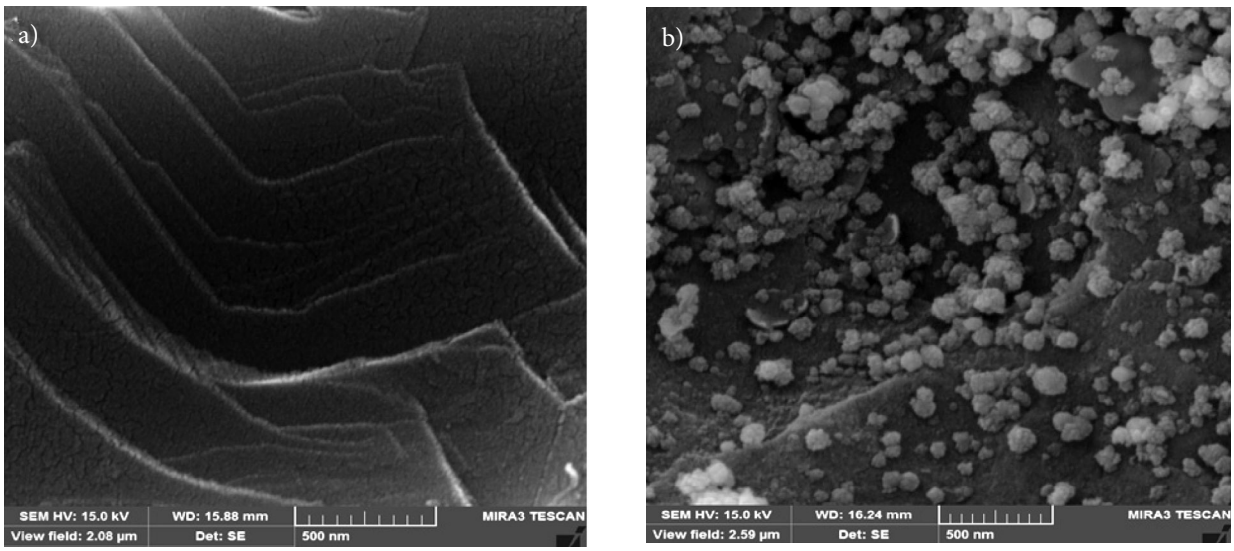

Figure 3. SEM images of (a) pure GO and (b) $Ag/CuFe_2O_4$/rGO nanocomposite.

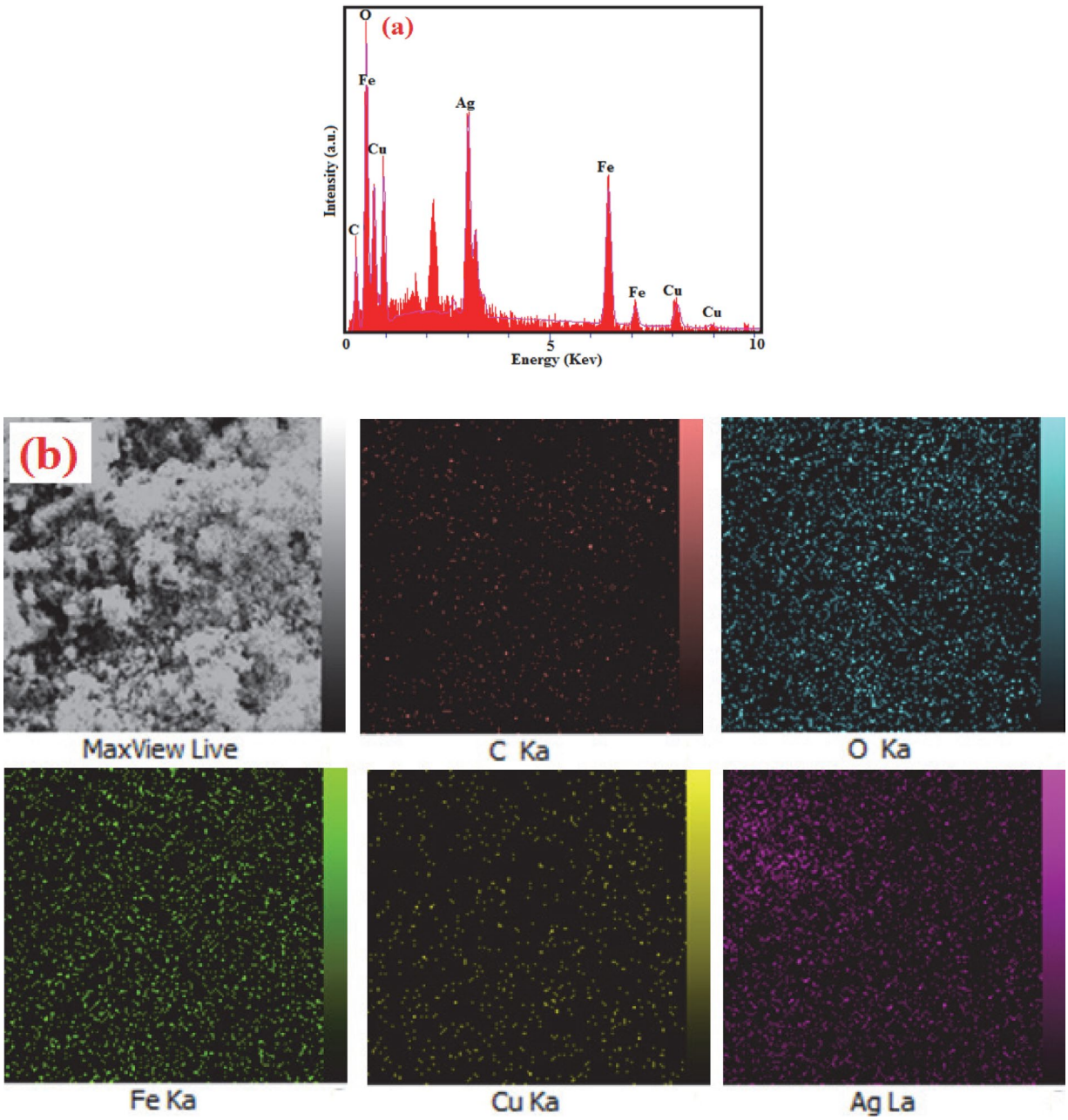

Figure 4. (a) EDX spectrum and (b) a representative SEM image with corresponding EDX elemental mappings of the Ag/$CuFe_2O_4$/rGO nanocomposite.

spectrum as shown in Figure 4(a). Figure 4(b) shows a representative SEM image of the nanocomposite with corresponding EDX elemental mappings. The distribution of corresponding elemental mappings confirmed that the elements were uniformly distributed over the nanocomposite, confirming the homogeneity of the sample. The EDX results further indicated that the Ag and $CuFe_2O_4$ nanoparticles were successfully loaded on the surface of rGO.

Figure 5 shows the TEM images of Ag/$CuFe_2O_4$ and Ag/$CuFe_2O_4$/rGO samples. Figure 5(a) shows the typical TEM image of the Ag/$CuFe_2O_4$, displaying that the sample consists of a large quantity of nearly uniform spheres nanoparticles which loosely aggregated. As can be seen in Figure 5(b), the almost transparent graphene sheets are fully exfoliated and decorated homogeneously with Ag and $CuFe_2O_4$ nanoparticles having an average diameter of 30 nm in consistent with the average particle size calculated from Debye-Scherer formula. No obvious aggregation was seen in Figure 5(b). The rGO sheets could not only prevent agglomeration of the Co_3O_4 nanoparticles and enable a good dispersion of these spherical particles, but also substantially enhance the specific surface area of the composite.

Raman analysis is a powerful technique to monitor significant structural changes of GO nanostructures

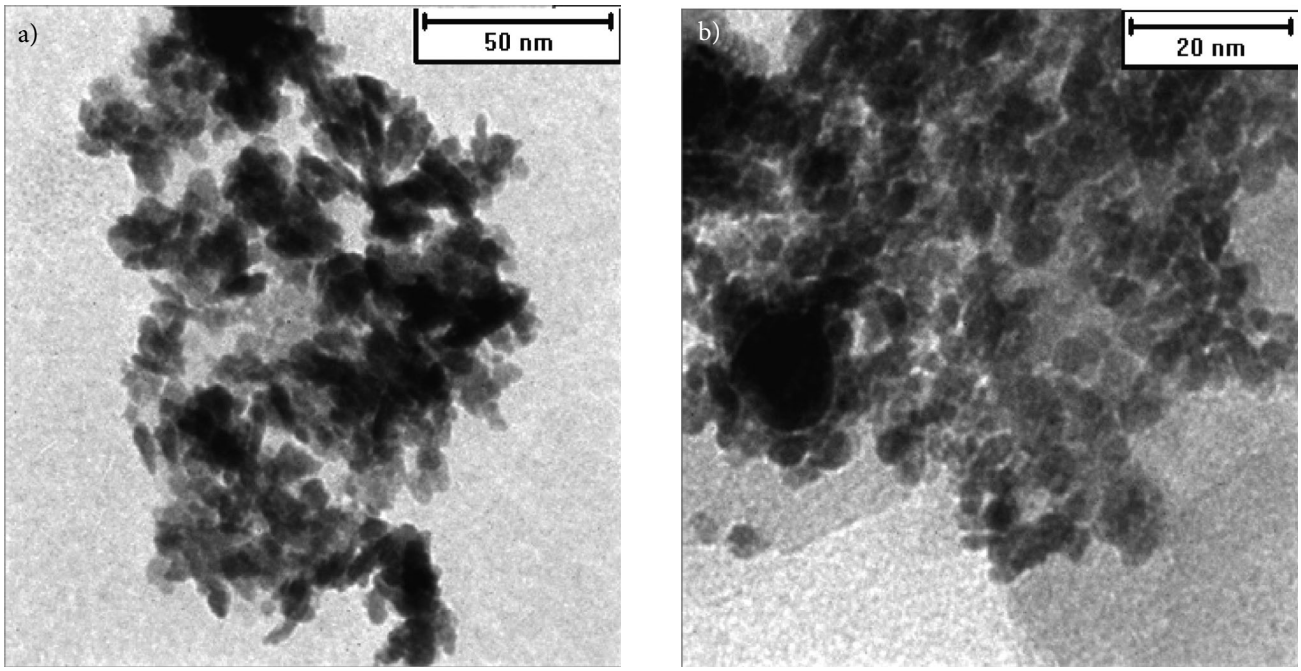

Figure 5. TEM images of (a) $Ag/CuFe_2O_4$ and (b) $Ag/CuFe_2O_4$/rGO nanocomposite.

during the reduction and composite formation. Figure 6 presents the Raman spectra of GO, rGO and $Ag/CuFe_2O_4$/rGO nanocomposite samples. Figure 6(a) and (b) shows the Raman spectra of the pure GO and GO sample after its reduction in EG solvent under hydrothermal conditions.

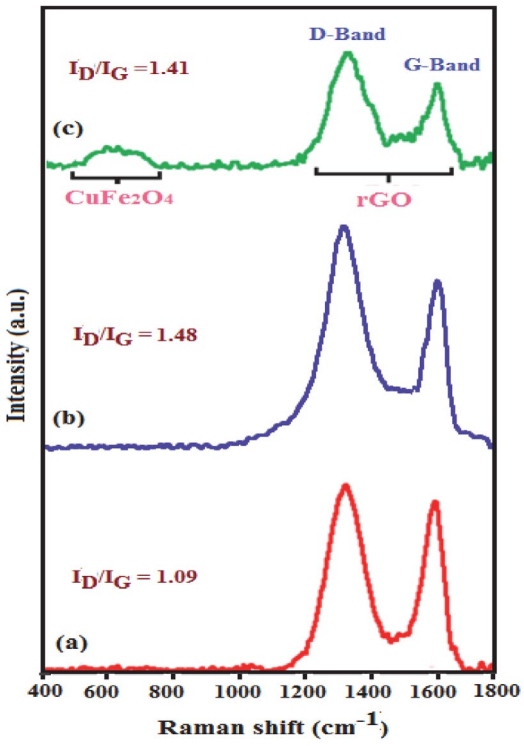

Figure 6. Raman spectra of (a) GO, (b) rGO and (c) $Ag/CuFe_2O_4$/rGO.

According to the Raman spectra of GO and rGO, the two characteristic bands at about 1318 and 1589 cm^{-1} can be attributed to the disordered structure (D band, sp^3 carbon atoms of disorders and defects) and graphitic structure (G band, sp^2 carbon atoms in graphitic sheets) of GO nanosheets, respectively.[46] As can be seen in Figure 6(c), the D and G bands still exist in the Raman spectrum of $Ag/CuFe_2O_4$/rGO composite, besides a broad band around 600 cm^{-1} related to the A_1g stretching vibrartion of Fe-O bond in the FeO_6 groups of $CuFe_2O_4$ nanoparticles.[47] Then, this finding demonstrates the coexistence of $CuFe_2O_4$ and rGO in the nanocomposite. Compared to pure GO and rGO samples, the position of D and G bands slightly shifted likely due to the strong interaction of the Ag and $CuFe_2O_4$ nanoparticles with the rGO nanosheets. Furthermore, the D band to G band intensity ratios for rGO (I_D/I_G = 1.48) and $Ag/CuFe_2O_4$/rGO (I_D/I_G = 1.41) are larger compared with that of pure GO (I_D/I_G = 1.09), which can be attributed to the increase in the degree of disorder and defects, and also the decrease in the average size of sp^2 domains.[48] The increase in the I_D/I_G ratio also confirms that the GO has been deoxygenated and reduced to rGO.

The magnetic properties of $CuFe_2O_4$ and $Ag/CuFe_2O_4$/rGO samples were examined using a vibrating sample magnetometer (VSM) at ambient temperature. From Figure 7(a) and (b), the saturation magnetizations (Ms) of the $CuFe_2O_4$ and $Ag/CuFe_2O_4$/rGO were found to be 68 emu/g and 48.2 emu g^{-1}, respectively. The slope defined as S-like shape of the magnetic hysteresis loops as well as the fact that both materials exhibit zero coercivity (Hc) and very low remanence (Mr) at ambient tempera-

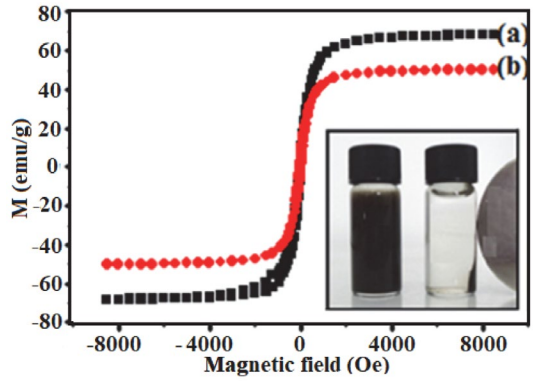

Figure 7. Magnetic hysteresis loops of (a) pure $CuFe_2O_4$ and (b) Ag/$CuFe_2O_4$/rGO at room temperature. The inset image shows the Ag/$CuFe_2O_4$/rGO suspension in the absence and presence of an external magnetic field.

ture allowed ranking them as superparamagnetic.[49] The lower range of magnetization (emu g^{-1}) for the Ag/$CuFe_2O_4$/rGO can be related to the decrease of $CuFe_2O_4$ content due to the presence of non-magnetic components (silver and graphene) in the nanocomposite. From the inset Figure 7, it is evident that homogeneous black Ag/$CuFe_2O_4$/rGO suspension can be easily separated from solution under an external magnet influence.

Figure 8 shows the nitrogen adsorption–desorption isotherms and corresponding pore size distributions curves (the inset) of rGO and Ag/$CuFe_2O_4$/rGO samples. As seen in Figure 8(a) and (b), the isotherms of GO and Ag/$CuFe_2O_4$/rGO nanocomposite can be classified to type-IV with H_4-type hysteresis loop for rGO and H_3-type hysteresis loop for the nanocomposite at high relative pressures according to the IUPAC classification, which indicate the presence of mesopores.[50] The BET surface area (S_{BET}) of the Ag/$CuFe_2O_4$/rGO nanocomposite is 90.20 m^2/g with the total pore volume of 0.261 cm^3/g, which are greater than the values of rGO (S_{BET} = 79.15 m^2/g and total pore volume = 0.123 cm^3/g). It can be concluded that immobilizing Ag and $CuFe_2O_4$ nanoparticles on the suface of graphene nanosheets increases the surface area and porosity which are favorable factors for improving the catalytic and adsorption performances.

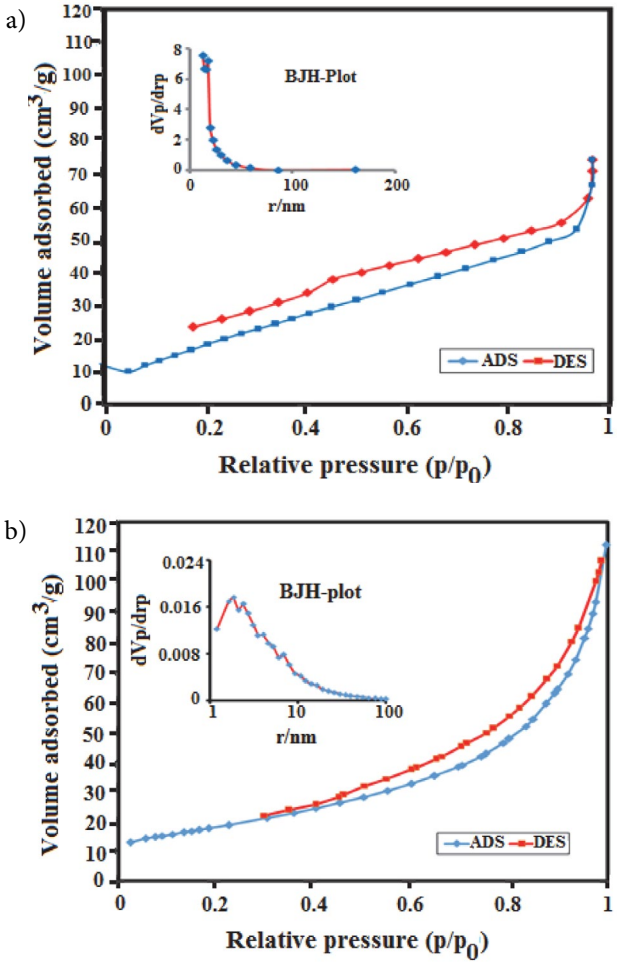

Figure 8. N_2 adsorption-desorption isotherms and pore-size distribution curves (the insets) of (a) rGO and (b) the Ag/$CuFe_2O_4$/rGO nanocomposite .

3. 2. Catalytic Reduction of Nitroarenes over the Ag/$CuFe_2O_4$/rGO Nanocomposite

The catalytic activity of the Ag/$CuFe_2O_4$/rGO nanocomposite was evaluated for the reduction of 2-nitroaniline (2-NA), 4-nitroaniline (4-NA), 2-nitrophenol (2-NP) and 4-nitrophenol (4-NP) in the presence of sodium borohydride ($NaBH_4$). In the reduction process, the initial concentrations of $NaBH_4$ and nitroaromatics were 20 mM and 0.2 mM, respectively. Figure 9(a)-(d) shows the typical UV-visible spectra and concentration changes of nitroaromatic compounds in the presence of Ag/$CuFe_2O_4$/rGO nanocomposite and $NaBH_4$. All compounds have an absorbance peak at about 400 nm under alkaline conditions.[51–56] The intensity of this peak decreases when the reduction proceeds in the presence of Ag/$CuFe_2O_4$/rGO nanocatalyst. The characteristic absorption peaks of 2-NA, 4-NA, 2-NP and 4-NP were disappeared in 25, 30, 10 and 15 min, respectively. Since the reductive reactions were carried out under the same experimental conditions, the different rates can be related to the structures of organic compounds. The pseudo first-order kinetics can be applied to evaluate the rate constants in the reduction process, because the concentration of $NaBH_4$ is higher compared to that of nitroarenes and it can be considered as a constant during the reaction time. The concentration of mentioned compounds at time t is defined as C_t and the initial concentration of them at t = 0 is regarded as C_0. The C_t/C_0 is measured from the relative intensity of absorbance (A_t/A_0). As shown in the insets of Figure 9(a)-(d), the linear relationship of $\ln[A]/[A_0]$ versus time (t) indicates that the reduction of nitrophenols and nitroanilines over Ag/$CuFe_2O_4$/rGO nanocomposite follows the pseudo first-order kinetics.

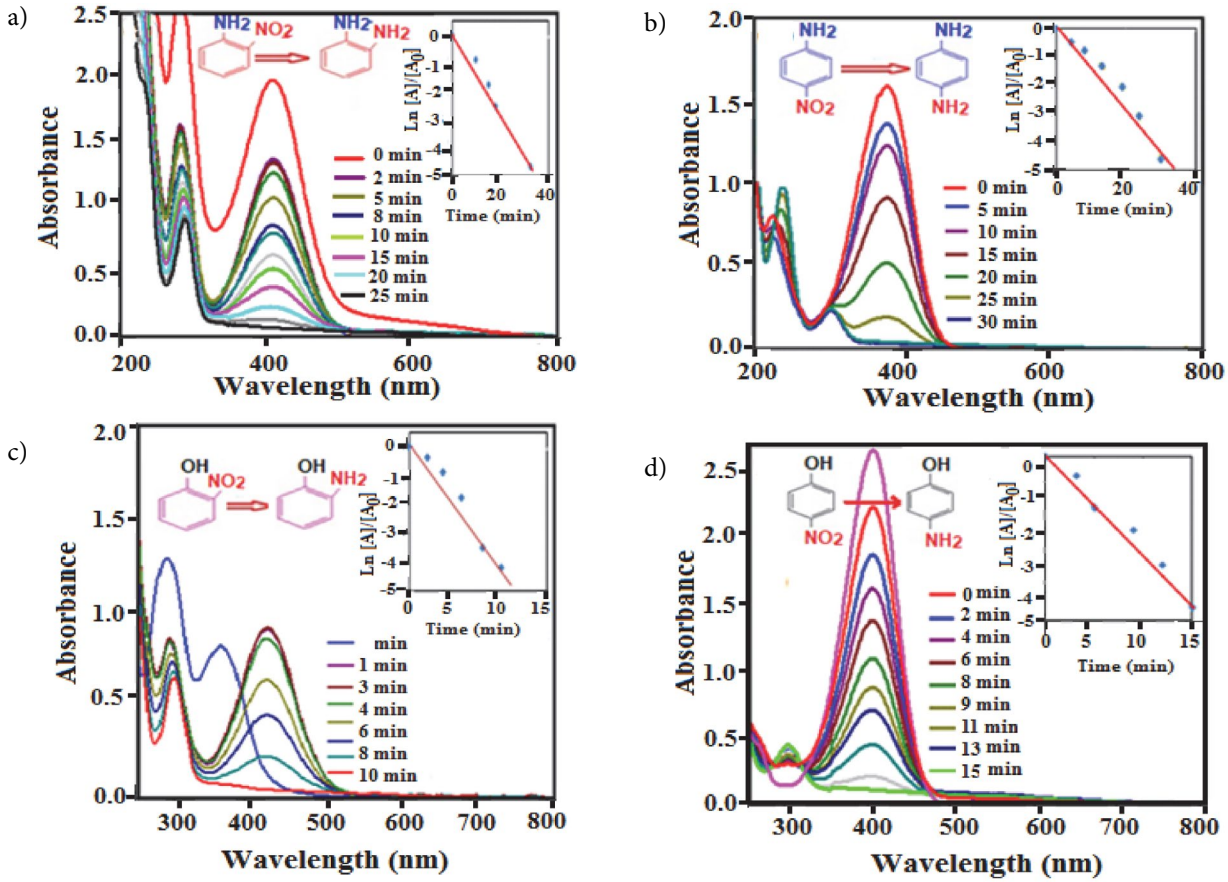

Figure 9. UV–visible absorption spectra of reaction solutions containing (a) 2-nitroaniline (b) 4-nitroaniline (c) 2-nitrophenol (d) 4-nitrophenol. The insets show plots of $\ln[A]/[A_0]$ against time.

As shown in Figure S1 (Supporting Information (SI)) $Ag/CuFe_2O_4$, Ag/rGO and $CuFe_2O_4$/rGO samples showed lower activity for the reduction of 4-NP compared to the ternary $Ag/CuFe_2O_4$/rGO nanocomposite, and they could not be regarded as effective catalysts for this reaction. Moreover, no considerable change in the ab-

Table 1. Comparison of the results obtained for the reduction of 4-NP in the present work with those obtained by some reported catalysts.

Entry	Catalyst	Conditions	Time	Ref.
1	Ni-PVA/SBA-15	H_2O, $NaBH_4$, r.t.	85 min	[57]
2	Hierarchical Au/CuO NPs	H_2O, $NaBH_4$, r.t	80 min	[58]
3	Cu NPs	THF/H_2O, $NaBH_4$, 50 °C	2 h	[59]
4	PdCu/graphene	EtOH/H_2O, $NaBH_4$, 50 °C	1.5 h	[60]
5	Au-GO	H_2O, $NaBH_4$, r.t.	30 min	[61]
6	$CoFe_2O_4$ NPs	H_2O, $NaBH_4$, r.t.	50 min	[62]
7	$FeNi_2$ nano-alloy	H_2O, $NaBH_4$, r.t	60 min	[63]
8	$NiCo_2$ nano-alloy	H_2O, $NaBH_4$, r.t.	30 min	[64]
9	CdS/GO	H_2O, $NaBH_4$, r.t.	30 min	[65]
10	dumbbell-like CuO NPs	H_2O, $NaBH_4$, r.t.	12 min	[66]
11	Ni NPs	H_2O, $NaBH_4$, r.t.	16 min	[67]
12	$CuFe_2O_4$ NPs	H_2O, $NaBH_4$, r.t.	14 min	[68]
13	Au NPs	H_2O, $NaBH_4$, r.t.	4 min	[69]
14	Pd/RGO/Fe_3O_4 NPs	H_2O, $NaBH_4$, r.t.	1 min	[70]
15	Cu/Fe_3O_4 NPs	H_2O, $NaBH_4$, r.t.	55 sec	[71]
16	Cu NPs/Perlite	H_2O, $NaBH_4$, r.t.	2.5 min	[72]
17	$Ag/CuFe_2O_4$/GO	H_2O, $NaBH_4$, r.t.	15 min	This work

sorbance band of 4-NP at 400 nm was observed in the absence of $Ag/CuFe_2O_4$/rGO, confirming that the reduction is mostly catalyzed by the $Ag/CuFe_2O_4$/rGO nanocomposite. In the presence of $Ag/CuFe_2O_4$/rGO nanocomposite and $NaBH_4$, the nitroarenes are easily reduced in aqueous solutions.

The study of the reaction mechanism helps to design a catalyst with better output. Figure S2 shows the catalytic mechanism of 4-NP reduction by the $Ag/CuFe_2O_4$/rGO nanocomposite in the presence of $NaBH_4$. During the hydrogenation reduction process, BH_4^- and 4-NP are first adsorbed on the surface of the catalyst, and then the Ag nanoparticles transfer electrons from BH_4^- to 4-NP, leading to the production of 4-aminophenol (4-AP).[21] After the reaction is completed, the $Ag/CuFe_2O_4$/rGO nanocatalyst can be separated easily from the solution by a magnet and applied for next reaction.

The obtained results in the reduction of 4-NP with $NaBH_4$ over the $Ag/CuFe_2O_4$/rGO nanocatalyst were compared with some reported catalysts in the literature (Table 1).[57–72] It is clear that with respect to the reaction conditions and/or reaction times, the present method is more suitable and/or superior (Table 1, entries 1-9). The reaction in the presence of most reported catalysts required longer reaction times. However, compared with some these reports, the $Ag/CuFe_2O_4$/rGO catalyst also presented close or lower catalytic activity for the reduction of 4-NP (Table 1, entries 10–16). Nevertheless, the $Ag/CuFe_2O_4$/rGO can be easily prepared and reused without the use of harsh, toxic and expensive chemicals which is very important in practical applications.

3. 3. Adsorption Performance of the $Ag/CuFe_2O_4$/rGO Nanocomposite

There are some methods on the effective elimination of hazardous substances from aqueous solutions, such as photo and sonocatalytic degradation, oxidation and adsorption that among them, adsorption is a good choice due to its higher efficiency and simpler operation.[73] In this context, considering the structure of the packed sp^2-bonded carbon atoms of rGO and magnetic property of $CuFe_2O_4$, it is expected that the $Ag/CuFe_2O_4$/rGO can be used as a novel and effective adsorbent for the removal of organic aromatic pollutants from wastewaters. The adsorption capacity was evaluated using two dyes: positively charged methylene blue (MB) and negatively charged methyl orange (MO). As indicated in Figure 10(a), the

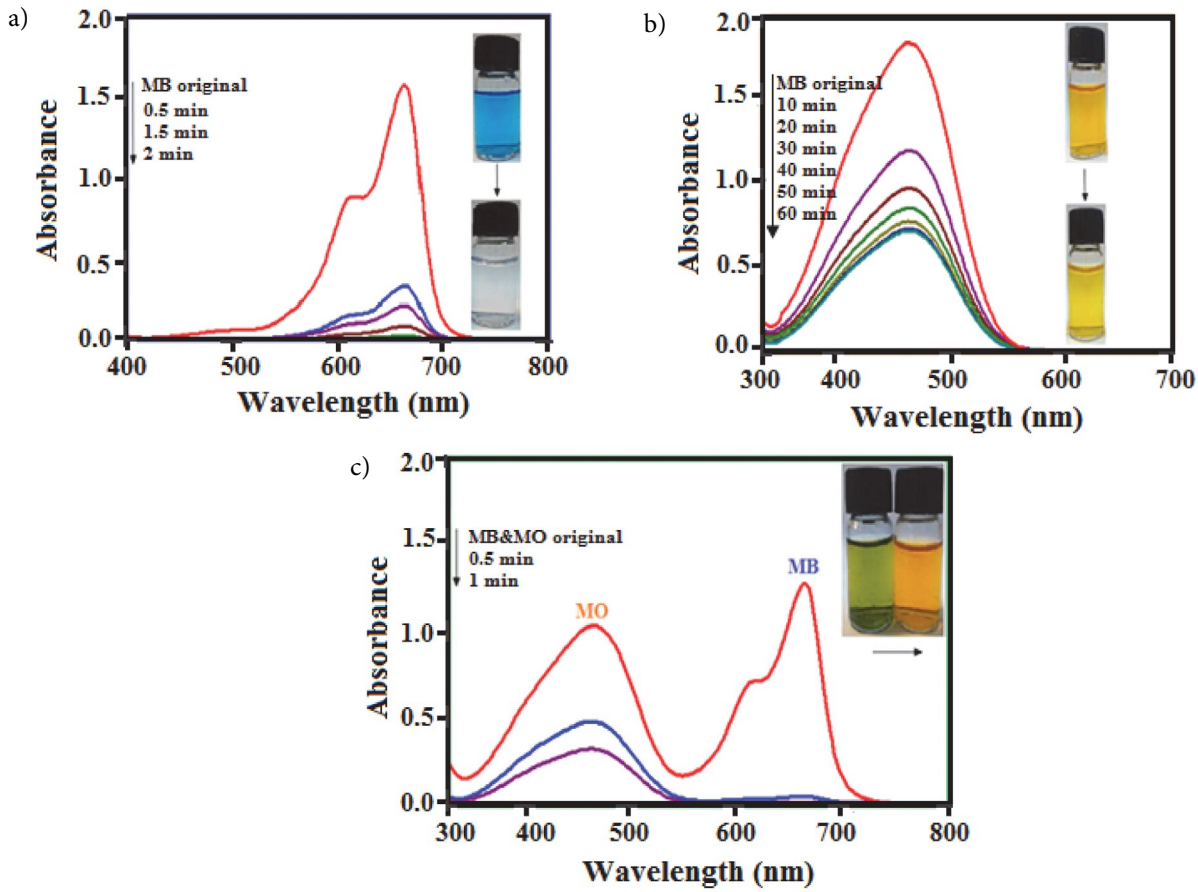

Figure 10. The adsorption capacity of $Ag/CuFe_2O_4$/rGO toward different organic dyes: (a) MB, (b) MO and (c) mixed dyes (MB + MO). Experimental conditions: dosage of adsorbent = 50 mg, [dye] = 25 mg/L, temperature = 25 °C and pH=7.

characteristic UV-vis absorption band of MB at 664 nm, decreased and disappeared within only 2 min. The extraordinary removal of MB could be largely ascribed to the π-π stacking between dyes and rGO nanosheets.[40] The electrostatic interactions between the positively charged dye and negatively charged residual oxygen-containing functional groups of rGO, were also effective in the adsorption process. The $Ag/CuFe_2O_4$ nanaoparticles could be acted as spacers to minimize the agglomeration of the rGO nanosheets. The adsorption ability of $Ag/CuFe_2O_4$/rGO nanocomposite towards MO dye was also investigated (Figure 10(b)). From the figure, the absorbance of MO at 463 nm decreased slightly after 60 min and the removal efficiency of MO was about 61%. Moreover, to confirm the ability of the $Ag/CuFe_2O_4$/rGO nanocomposite to separate MB and MO dye molecules, a mixed dye solution was selected to determine the selective adsorption capacity of the solid composite. From Figure 10(c), the absorption peak of MB disappeared quickly; just leaving the absorption peak of MO, indicating that $Ag/CuFe_2O_4$/rGO composite could selectively adsorb the cationic MB dye when exposed to the mixed solutions of MB+MO. The finding indicates that the $Ag/CuFe_2O_4$/rGO nanocomposite also possesses selective adsorption ability towards the cationic dyes in wastewater.

3. 3. 1. Effect of the Initial Concentration of MB

As shown in Figure 11(a), the effect of the initial concentration of MB solution on adsorption efficiency was studied. Accordingly to the obtained results, the adsorption percentage of the nanocomposite towards MB can reach up to about 100% at lower initial concentrations (15 and 25 and 75 mg/L). However, for MB with concentration of 100 mg/L, adsorption percentage decreased to 70% within 30 minutes and the $Ag/CuFe_2O_4$/rGO nanocomposite could not adsorb more dye molecules due to saturation of adsorption capacity.

3. 3. 2. Effect of Type of Adsorbent

Figure 11(b) represents the adsorption capacities of $Ag/CuFe_2O_4$, rGO and $Ag/CuFe_2O_4$/rGO samples toward MB dye. As seen, the removal efficiency of MB by rGO and $Ag/CuFe_2O_4$ nanoparticles are 78% and 25% respectively. The high adsorption performance of graphene sheets mainly is due to the large surface area and graphitized basal plane structure of it, which could provide excellent conditions for adsorption of dyes.[31] However, in the presence of $Ag/CuFe_2O_4$/rGO nanocomposite, the removal efficiency of MB is increased to 100% indicating the as-prepared nanocomposite is more suitable and superior. The Ag and $CuFe_2O_4$ nanoparticles on the surface of graphene prohibit the restacking of its layers and thus increase the surface area and adsorption capacity of the composite. This result is consistent with BET analyses.

3. 3. 3. Effect of Adsorbent Dosage

The influence of the adsorbent dosage on MB adsorption in Figure 11(c) indicates that with the increase of the adsorbent dosage from 25 to 35 mg, the removal efficiency of MB is enhanced to 78%, and when the dosage is 50 mg, it reaches 100% within 2 min. The finding indicates that 50 mg is the suitable dosage for the adsorption of 25mg/L MB solution.

3. 3. 4. Effect of pH

As shown in Figure 11(d), the initial solution pH plays an important role in the adsorption of MB on the surface of $Ag/CuFe_2O_4$/rGO nanocomposite. The adsorption of MB increases gradually as pH value increases from 2 to 7 and finally maintains the high level with increasing pH. In acidic pHs, the surface of $Ag/CuFe_2O_4$/rGO nanocomposite is positively charged due to protonation reaction. Thus, the electrostatic repulsion between positively charged MB dye and $Ag/CuFe_2O_4$/rGO nanocomposite leads to the low adsorption of MB in this pH range. However, at pH ≥ 7, the surface of the adsorbent is negatively charged and more available to retain the cationic MB dye, resulting in the increase of MB adsorption. In the pH range of 7-11, the removal of MB reaches maximum and remains approximately constant.

3. 3. 5. Recyclability of the $Ag/CuFe_2O_4$/rGO Nanocomposite

To evaluate the stability and reusability of the $Ag/CuFe_2O_4$/rGO nanocomposite which are important factors for practical applications, recycling experiments were performed. The composite was separated from the reaction mixture by an external magnet after the first use in the adsorption of MB and washed thoroughly with ethanol. The recovered nanocomposite was found to be reusable for at least five runs without significant loss in activity. As shown in Figure S3, the slight decrease of performance could be observed after five runs.

The amounts of Ag and Cu metals in aqueous solution after each run were analyzed by ICP-AES. It was shown that the leaching of these metals from the catalyst is negligible, confirming the stability of the composite. Furthermore, the structural stability was investigated by XRD, FT-IR, EDX and SEM analyses after five runs. As shown in Figure S4, these results did not show significant change after the fifth run in comparison with those of the fresh sample.

4. Conclusions

In summary, the $Ag/CuFe_2O_4$/rGO nanocomposite was prepared through a facile one-top solvothermal route. The $Ag/CuFe_2O_4$ nanoparticles were loaded on the surface

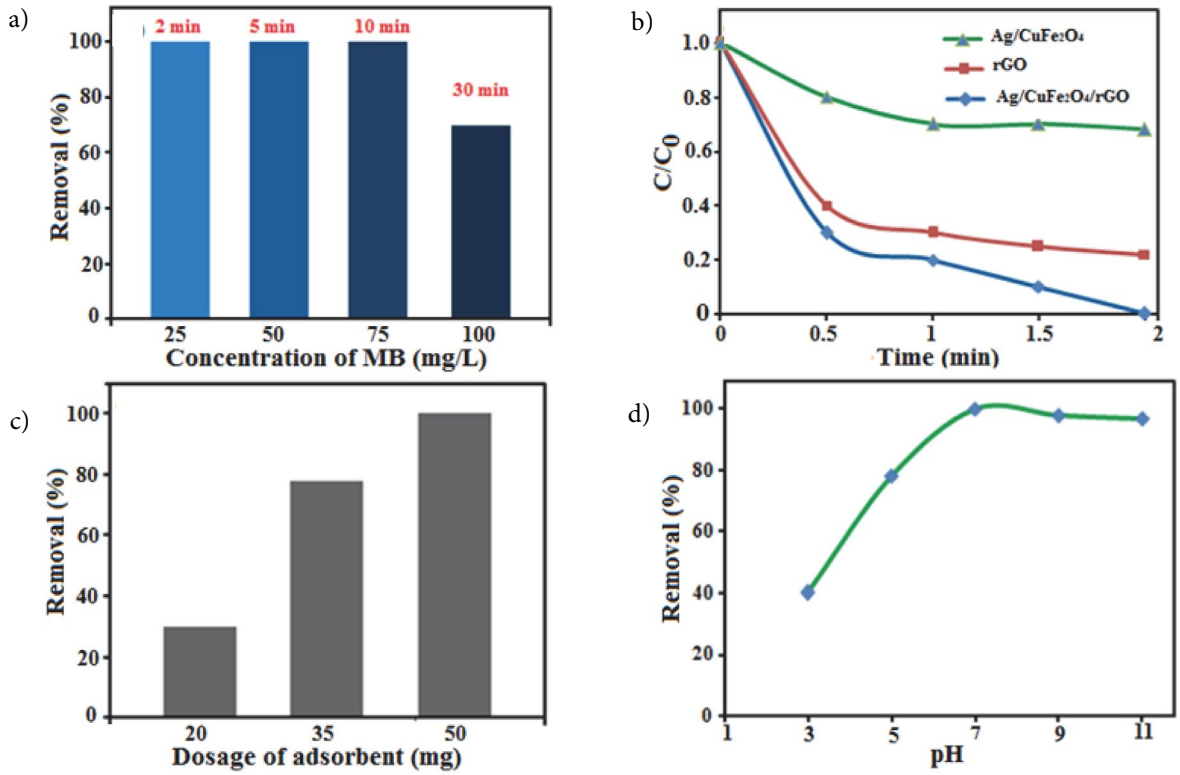

Figure 11. The adsorption capacity of the $Ag/CuFe_2O_4$/rGO nanocomposite toward MB solutions with different values of (a) concentration of dye, (b) type of adsorbent, (c) dosage of adsorbent and (d) pH.

of GO and the nanocomposite displayed magnetic property. The catalytic performance of this composite was excellent for reduction of nitroarenes in the presence of $NaBH_4$. The adsorption capacity of MB and MO dyes was also investigated and indicated that the removal efficiency of MB was 100% within only 2 min. Interestingly, due to the fast adsorption of MB molecules, the $Ag/CuFe_2O_4$/rGO nanocomposite could be used as effective and selective adsorbent for the removal of MB molecules from the mixed MB+MO dye solution. The $Ag/CuFe_2O_4$/rGO was separated from solution for reusing by simply applying an external magnetic field. Results obtained in this work open a way to the fabrication of effective nanomaterials for serving as an ideal platform to study the various heterogeneous catalytic processes and wastewater purification.

5. Acknowledgements

The authors gratefully acknowledge the Lorestan University Research Council and Iran Nanotechnology Initiative Council (INIC) for their financial supports.

6. References

1. Y. Wu, M. Wen, Q. Wu and H. Fang, *J. Phys. Chem. C*, **2014**, *118*, 6307–6313. **DOI:**10.1021/jp412711b
2. Y. Lu, Y. Mei, M. Ballauff and M. Drechsler, *J. Phys. Chem.* B, **2006**, *110*, 3930–3937. **DOI:**10.1021/jp412711b
3. Z. Jiang, J. Xie, D. Jiang, J. Jing and H. Qin, *CrystEngComm*., **2012**,*14*, 4601. **DOI:**10.1039/c2ce25205h
4. A. Saha and B. Ranu, *J. Org. Chem*., **2008**, *73*, 6867–6870. **DOI:**10.1021/jo800863m
5. S. Gosh, *Appl. Catal. A: Gen*., **2004**, *268*,61–66. **DOI:**10.1016/j.apcata.2004.03.017
6. S. Zhou, M. Wen, N. Wang, Q. Wu, Q. Wu and L. Cheng, *J. Mater. Chem*., **2012**, *22*, 16858–16864. **DOI:**10.1039/c2jm32397d
7. G. Wienhöfer, I. Sorribes, A. Boddien, F. Westerhaus, K. Junge, H. Junge, R. Llusar and M. Beller, *J. Am. Chem. Soc*., **2011**, *133*, 12875–12879.
8. S. Farhadi and F. Siadatnasab, *Chin. J. Catal.*, **2016**, *37*,1487–1495. **DOI:**10.1016/S1872-2067(16)62473-7
9. S. Karthikeyan, V. K. Gupta, R. Boopathy, A. Titus and G. Sekaran, *J. Mol. Liq*., **2012**, *173*, 153–163. **DOI:**10.1016/j.molliq.2012.06.022
10. Y. Liu, C. Luo, J. Sun, H. Li, Z. Sun and S. Yan, *J. Mater. Chem.* A., **2015**, *3*, 5674–5682. **DOI:**10.1039/C4TA07112C
11. L. Zhang, B. Shan, H. Yang, D. Wu, R. Zhu, J. Nie and R. Cao, *RSC Adv*., **2015**, *5*, 23556–23562.
12. P. Chowdhury and T. Viraraghavan, *Sci. Total Environ*., **2009**, *407*, 2474–2492. **DOI:**10.1016/j.scitotenv.2008.12.031
13. F.-J. Ma, S.-X. Liu, C.-Y. Sun, D.-D. Liang, G.-J. Ren, F. Wei, Y.-G. Chen and Z.-M. Su, *J. Am. Chem. Soc*., **2011**, *133*, 4178–4181. **DOI:**10.1021/ja109659k

14. M. Y. Zhu, D. H. Meng, C. J. Wang, J. Di and G. W. Diao, *Chin. J. Catal*., **2013**, *34*, 2125–2129. **DOI:**10.1016/S1872-2067(12)60717-7
15. J. J. Yan, K.Wang, H. Xu, J. Qian, W. Liu, X. W.Yang and H. M. Li, *Chin. J. Cata*l., **2013**, *34*, 1876–1882. **DOI:**10.1016/S1872-2067(12)60677-9
16. R. K. Narayanan and S. J. Devaki, *Ind. Eng. Chem. Res.*, **2015**, *54*, 1197–1203. **DOI:**10.1021/ie5038352
17. K. R. Gopidas, J. K. Whitesell and M. A. Fox, *Nano Lett.*, **2003**, *3*, 1757–1760. **DOI:**10.1021/nl0348490
18. R. Narayanan and M. A. El-Sayed, *J. Am. Chem. Soc*., **2003**, *125*, 8340–8347. **DOI:**10.1021/ja035044x
19. T. T. Nge, M. Nogi and K. Suganuma, *J. Mater. Chem*. C, **2013**, *1*, 5235–5243. **DOI:**10.1039/c3tc31220h
20. S. J. Devaki, R. K. Narayanan and S. Sarojam, *Mater. Lett.*, **2014**, *116*, 135–138. **DOI:**10.1016/j.matlet.2013.10.110
21. F. Lin and R. Doong, *J. Phys. Chem*. C, **2011**, *115*, 6591–6598. **DOI:**10.1021/jp110956k
22. C. Xu, J. Xie, D. Ho, C. Wang, N. Kohler, E. G. Walsh, J.R. Morgan, Y. E. Chin and S. Sun, *Angew. Chem. Int. Ed.,* **2008**, *47*, 173–176. **DOI:**10.1002/anie.200704392
23. M.S. Chen, *Science.* **2004**, *306,* 252–255. **DOI:**10.1126/science.1102420
24. M. Comotti, W.-C. Li, B. Spliethoff and F. Schüth, *J. Am. Chem. Soc*., **2006**, *128*, 917–924. **DOI:**10.1021/ja0561441
25. S. Tang, S. Vongehr and X. Meng, *J. Mater. Chem*., **2010**, *20*, 5436. **DOI:**10.1039/c0jm00456a
26. A. K. Geim and K. S. Novoselov, *Nat. Mater*., **2007**, *6*, 183–191. **DOI:**10.1038/nmat1849
27. S. Zhang,Y. Y. Shao, H. G. Liao, I. A. Aksay, G. P. Yin and Y. H. Lin, *Chem. Mater*., **2011**, *23*, 1079–1081. **DOI:**10.1021/cm101568z
28. R. S. Weatherup, C. Baehtz, B. Dlubak, B. C. Bayer, P. R. Kidambi, R. Blume, R. Schloegl and S. Hofmann, *Nano Lett*., **2013**, *13*, 4624–4631. **DOI:**10.1021/nl401601x
29. Y. Wenzhu and C. Huaqiang, *RSC Adv.*, **2016**, *6*, 100636–100642.
30. H. M. Sun, L. Y. Cao and L. H. Lu, *Nano Res*., **2011**, *4*, 550–62. **DOI:**10.1007/s12274-011-0111-3
31. S.Wang, J. Wei, S. Lv, Z. Guo and F. Jiang, *Clean – Soil, Air, Water*, **2013**, 41, 992–1001. **DOI:**10.1002/clen.201200093
32. Y. J. Xu, G. Weinberg, X. Liu, O. Timpe, R. Schlogl and D. S. Su, *Adv. Funct. Mater*., **2008**, 18, 3613–3619. **DOI:**10.1002/adfm.200800726
33. T. Zhu, J. S. Chen and X. W. Lou, *J. Phys. Chem. C*, **2012**, 116, 6873–6878. **DOI:**10.1021/jp300224s
34. M. Valix, W. H. Cheung and G. Mckay, *Langmuir*, **2006**, 22, 4574–4582. **DOI:**10.1021/la051711j
35. N. K. Lazaridis, G. Z. Kyzas, A. A. Vassiliou and D. N. Bikiaris, *Langmuir*, **2007**, 23, 7634–7643. **DOI:**10.1021/la700423j
36. Z. Hasan and S. H. Jhung, *J. Hazard. Mater*., **2015**, 283, 329–339. **DOI:**10.1016/j.jhazmat.2014.09.046
37. W. Lv, D.-M. Tang, Y.-B. He, C.-H. You, Z.-Q. Shi, X.-C. Chen, C.-M. Chen, P.-X. Hou, C. Liu and Q.-H. Yang, *ACS Nano*, **2009**, *3*, 3730–3736. **DOI:**10.1021/nn900933u
38. Y. Fu, J. Wang, Q. Liu and H. Zeng, *Carbon*, **2014**, *77*, 710–721. **DOI:**10.1016/j.carbon.2014.05.076
39. H. Yanga, J. Yana, Z. Lua, X. Chenga and Y. Tang, *J. Alloys Compd.,* **2009**, *476*, 715–719. **DOI:**10.1016/j.jallcom.2008.09.104
40. G. Liu, w. Jiangn, Y. Wang, S. Zhong, D. Sun, J. Liu and F. Li, *Ceram.Inter.*, **2015**, *41*, 4982–4988. **DOI:**10.1016/j.ceramint.2014.12.063
41. J. Wang, T. Tsuzuki, B. Tang, X. Hou, L. Sun and X. Wang, *ACS Appl. Mater. Interfaces,* **2012**, *4*, 3084–3090. **DOI:**10.1021/am300445f
42. C. Zhu, S. Guo, P. Wang, L. Xing, Y. Fang, Y. Zhai and S. Dong, *Chem. Commun*., **2010**, *46*, 7148–7150. **DOI:**10.1039/c0cc01459a
43. J. E. Tasca, A. Ponzinibbio, G. Diaz, R. D. Bravo and A. Lavat and M. G. González, *Top. Catal*., **2010**, *53*, 1087–1090. **DOI:**10.1007/s11244-010-9538-0
44. S. Hashemian , M. Rahimi and A. A. Kerdegari, *Desalin. Water Treat*.,**2015**,57, 14696–14707 **DOI:**10.1080/19443994.2015.1065766
45. Z.-H. Huang, G. Liu and F. Kang, *ACS Appl. Mater. Interfaces*, **2012**, *4*, 4942–4947. **DOI:**10.1021/am3013104
46. Y. Sun, D. Shao, C. Chen, S. Yang and X. Wang, *Environ. Sci. Technol*., **2013**, *47*, 9904–9910. **DOI:**10.1021/es401174n
47. Y. Fu, Q. Chen, M. He, Y. Wan, X. Sun, H. Xia and X. Wang, *Ind. Eng. Chem. Res*., **2012**, *51*, 11700–11709. **DOI:**10.1021/ie301347j
48. S. Bai, X. Shen, X. Zhong, Y. Liu, G. Zhu, X. Xu and K. Chen, *Carbon*, **2012**, *50*, 2337–2346. **DOI:**10.1016/j.carbon.2012.01.057
49. A. S. K. Kumar and S. J. Jiang, *J. Mol. Liq.* **2017**, *237*, 387–401. **DOI:**10.1016/j.molliq.2017.04.093
50. K. Pourzare, S. Farhadi and Y. Mansourpanah, *Acta Chim. Slov.*, **2017**, *64*, 945–958. **DOI:**10.17344/acsi.2017.3642
51. Y. Deng, Y. Cai, Z. Sun, J. Liu, C. Liu, J. Wei, W. Li, C. Liu, Y. Wang and D. Zhao, *J. Am. Chem.* Soc., **2010**, *132*, 8466–8473. **DOI:**10.1021/ja1025744
52. N. Pradhan, A. Pal and T. Pal, *Eng. Asp*., **2002**, *196*, 247–257. **DOI:**10.1016/S0927-7757(01)01040-8
53. S. Jana, S. Ghosh, S. Nath, S. Pande, S. Prahraj, S. Panigrahi, S. Basu, T. Endo and T. Pal, *Appl. Catal. A: Gen*., **2006**, *313*, 41–48. **DOI:**10.1016/j.apcata.2006.07.007
54. Y. Zhu, J. Shen, K. Zhou, C. Chen, X. Yang and C. Li, *J. Phys. Chem. C*, **2011**, *115*, 1614–1619. **DOI:**10.1021/jp109276q
55. M. Wang, Y. Ni and A. Liu, *ACS Omega*, **2017**, 2, 1505–1512.
56. Y. Zhong, Y. Ni, S. Li and M. Wang, *RSC Adv*., **2016**, 6, 15831–15837.
57. R. J. Kalbasi, A. A. Nourbakhsh and F. Babaknezhad, *Catal. Commun.*, **2011**, *12*, 955–960. **DOI:**10.1016/j.catcom.2011.02.019
58. S. Y. Gao, X. X. Jia, Z. D. Li and Y. L. Chen, *J. Nanopart. Res.*, **2012**, *14*, 1–11.
59. Z. Duan, G. Ma and W. Zhang, *Bull. Korean Chem. Soc.*, **2012**, **33**, 4003–4006. **DOI:**10.5012/bkcs.2012.33.12.4003
60. A. K. Shil, D. Sharma, N. R. Guha and P. Das, *Tetrahedron Lett*., **2012**, *53*, 4858–4861. **DOI:**10.1016/j.tetlet.2012.06.132

61. Y. Choi, H. S. Bae, E. Seo, S. Jang, K. H. Park and B. S. Kim, *J. Mater. Chem.* **2011**, *21*, 15431–15436. **DOI:**10.1039/c1jm12477c
62. M. Nasrollahzadeh, M. Bagherzadeh and H. Karimi, *J. Colloid Interface Sci.*, **2016**, ***465***, 271–278. **DOI:**10.1016/j.jcis.2015.11.074
63. K. L. Wu, R. Yu and X. W. Wei, *Cryst. Eng. Commun.*, **2012**, 14, 7626–7632. **DOI:**10.1039/c2ce25457c
64. K. L. Wu, X. W. Wei, X. M. Zhou, D. H. Wu, X. W. Liu, Y. Ye and Q. Wang, *J. Phys. Chem. C,* **2011**, *115*, 16268–16274. **DOI:**10.1021/jp201660w
65. S. Liu, Z. Chen, N. Zhang, Z. R. Tang and Y. J. Xu, *J. Phys. Chem. C*, **2013**, *117*, 8251–8261. **DOI:**10.1021/jp400550t
66. W. Che, Y. Ni, Y. Zhang and Y. Ma, *J. Phys. Chem. Solids*, **2015**, *77*, 1–7. **DOI:**10.1016/j.jpcs.2014.09.006
67. D. Z. Jiang, J. Xie, D. Jiang, X. Wei and M. Chen, *Cryst. Eng. Comm.*, **2013**, *15*, 560–569. **DOI:**10.1039/C2CE26398J
68. J. Feng, L. Su, Y. Ma, C. Ren, Q. Guo and X. Chen, *Chem. Eng. J.* **2013**, *221*,16–24. **DOI:**10.1016/j.cej.2013.02.009
69. Q. Cui, B. Xia, S. Mitzscherling, A. Masic, L. Li, M. Bargheer and H. Möhwald, *Colloids Surf. A: Physicochem. Eng. Aspects*, **2015**, *465*, 20–25. **DOI:**10.1016/j.colsurfa.2014.10.028
70. M. Atarod, M. Nasrollahzadeh and S. M. Sajadi, *J. Colloid Interface Sci.*, **2016,** *465*, 249–258. **DOI:**10.1016/j.jcis.2015.11.060
71. M. Nasrollahzadeh, M. Atarod and S. M. Sajadi, *Appl. Surf. Sci.*, **2016**, *364*, 636–644. **DOI:**10.1016/j.apsusc.2015.12.209
72. M. Nasrollahzadeh and S. M. Sajadi, *Ceram. Inter.*, **2015**, *41*, 14435–14439. **DOI:**10.1016/j.ceramint.2015.07.079
73. A. Mahdizadeh, S. Farhadi and A. Zabardasti, *RSC Adv.*, **2017**, *7*, 53984–53995.

Povzetek

Z razmeroma enostavno solvotermalno sintezo smo pripravili ternarni magnetni nanokompozit Ag/$CuFe_2O_4$/rGO. Redukcija grafen oksida (GO) do reducirane zvrsti (rGO) in "in-situ" depozicija $CuFe_2O_4$ in nanodelcev Ag na rGO je potekala hkrati. Za določanje strukture, sestave in morfologije pripravljenega nanokompozita smo uporabili naslednje tehnike: infradrečo spektroskopijo (FT-IR), rentgensko praškovno difrakcijo (XRD), merilnik namagnetenosti s tresočim se vzorcem (VSM), vrstično elektronsko mikroskopijo s poljsko emisijo (FESEM), energijsko disperzijsko spektroskopijo rentgenskih žarkov (EDXS), presevno elektronsko mikroskopijo (TEM) in meritve površine (BET). Rezultati so pokazali, da so se nanodelci Ag in $CuFe_2O_4$ uspešno vezali na površino rGO. Katalitsko učinkovitost nanokompozita Ag/$CuFe_2O_4$/rGO smo določali z rekacijo redukcije nitroarenov do ustreznih aminov v prisotnosti natrijevega borohidrida ($NaBH_4$) kot reducenta. Nanokompozit je pokazal visoko učinkovitost pri redukcije nitroarenov s 100% konverzijo v 10-30 minutah. Katalitska aktivnost Ag/$CuFe_2O_4$/rGO je bila izboljšana v primerjavi z vzorci Ag/$CuFe_2O_4$, Ag/rGO in $CuFe_2O_4$/rGO zaradi lažjega prenosa elektronov. Poleg tega so podatki o adsorpciji pokazali, da lahko kationsko barvilo metilensko modro (MB) skoraj v celoti odstranimo z uporabo kompozita Ag/$CuFe_2O_4$/rGO v 2 minutah. Postopek je selektiven, kar smo preverili z uporabo kompozita za adsorpcijo barvila MB iz mešane raztopine z anionskim barvilom metil oranž (MO). Sestava nanokompozita, v katerem so tudi magnetni nanodelci $CuFe_2O_4$, nam omogoča, da lahko po uporabi kompozit enostavno ločimo in ponovno uporabimo.